J. Fluid Mech. (2005), *vol.* 540, *pp.* 75–97.
doi:10.1017/S0022112005003381 Printed in the United Kingdom

Shallow flow past a cylinder: transition phenomena at low Reynolds number

By H. FU AND D. ROCKWELL

Lehigh University, Department of Mechanical Engineering and Mechanics, 354 Packard Laboratory, 19 Memorial Drive West, Bethlehem, PA 18015, USA
dor0@lehigh.edu

(Received 23 February 2004 and in revised form 24 November 2004)

The unstable structure of the near wake of a vertical cylinder, in a fully developed laminar free-surface layer, is characterized in relation to the unsteadiness of the horseshoe (necklace) vortex system about the upstream surface of the cylinder. A cinema technique of high-image-density particle image velocimetry allows space–time imaging of the critical regions of the flow and thereby wholefield representations of patterns of the flow structure, in conjunction with spectra and cross-spectra at a large number of points over the flow domain.

The unsteadiness of the near wake was examined over a range of wake stability parameter $S = c_f D/h_w$, in which c_f is the bed friction coefficient, D is the cylinder diameter, and h_w is water depth; this range of S was selected such that the classical Kármán mode of vortex formation remained completely suppressed. Within this range, increase of the Reynolds number, based on depth h_w of the shallow layer and D of the cylinder, yielded the onset and development of an instability mode that takes the form of a varicose, as opposed to a sinuous, pattern of vortices. It is related to the unsteadiness of the horseshoe (necklace) vortex system on the upstream side of the cylinder. The process of vortex formation in the near wake is interpreted in terms of multiple, coexisting layers of vorticity due to both the horseshoe vortices and the vorticity layer associated with separation from the cylinder.

Furthermore, it is demonstrated that when the near wake is stable at sufficiently low values of the Reynolds number, based on depth h_w and cylinder diameter D, application of external perturbations via small-amplitude rotational oscillations of the cylinder, at the most unstable frequency of the separating shear layers, can lead to destabilization of the near wake in a sinuous mode of small-scale vortical structures. Moreover, this type of rotational perturbation of the cylinder, applied at the expected frequency of large-scale Kármán vortex formation, can also yield destabilization of the near wake in this mode. These types of perturbations lead to substantial alterations of the patterns of vorticity and streamline topology, as well as Reynolds stresses and entrainment velocities of the separating shear layers, along the bed, relative to patterns above the bed.

1. Introduction

1.1. *Previous related investigations*

The unstable wake of a cylinder in shallow flow has been the subject of a range of investigations in recent years. In essence, when shallow flow of effective depth h_w flows past a vertical obstacle or cylinder of diameter D, such that $D/h_w \gg 1$,

the wake is of a shallow form and can exhibit distinctive characteristics relative to the corresponding case of a wake of large spanwise extent, as defined in the images of Chen & Jirka (1995, 1997). Such shallow flows have been observed in nature in atmospheric, oceanographic and coastal flows, as described by Scorer (1978), Wolanski, Imberger & Heron (1984), Pattiaratchi, James & Collins (1986), Ingram & Chu (1987) and Smith & Grubisic (1993).

The existence of a large-scale instability in the near wake of a cylinder in shallow flow should account for the possible existence of either a global (absolute) or convective instability, as reviewed by Huerre & Monkewitz (1990) for wakes of large spanwise extent, the physics of which are assessed by Williamson (1996). For the corresponding shallow wake, not only the destabilizing effect of the transverse velocity gradient, i.e. transverse shear across the wake, but also the stabilizing influence of bed friction must be accounted for. Schar & Smith (1993), Grubisic, Smith & Schar (1995), and Chen & Jirka (1997) carried out global and absolute instability analyses for this class of shallow flows. Surface friction was neglected in the analysis of Schar & Smith (1993), while it was incorporated by Grubisic *et al.* (1995) in their absolute instability analysis involving approximation of the wake velocity profile. Chen & Jirka (1997) characterized the distinction between absolute and convective instabilities in the near wake and defined the criterion for transformation from a convectively unstable to stable wake.

Laboratory experiments, which address various aspects of unstable and stable near wakes, have been performed by Ingram & Chu (1987), Chen & Jirka (1995), Carmer, Weitbrecht & Jirka (2001), Carmer, Rummel & Jirka (2002, 2003), Akilli & Rockwell (2002), and Kahraman, Sahin & Rockwell (2002). Closely related works, which also provide insight into the structure of the near-wake instability, include characterization of concentration profiles in the shallow turbulent wake of a bluff body by Balachandar, Chu & Zhang (1997) and Balachandar, Tachie & Chu (1999), the wake of a flat plate in shallow flow investigated by Balachandar, Ramachandran & Tachie (2000) and Tachie & Balachandar (2001), and the unstable wake from a simulated island with finite side slope in steady and oscillatory flow by Lloyd & Stansby (1997) and Lloyd, Stansby & Chen (2001).

The possible unstable and stable modes of the near-wake structure can be related to a stability parameter $S = c_f D/h_w$, in which c_f is the quadratic bed friction coefficient, D is the diameter of the cylinder, and h_w is the depth of the shallow water layer. This form of the instability parameter, introduced by Ingram & Chu (1987) as an extension of the single shear layer criterion of Chu, Wu & Khayat (1983), and assessed in the context of global (absolute) and convective instabilities of the near wake by Chen & Jirka (1997), has served as an effective parameter in defining the demarcations between the wake modes, as summarized by Chen & Jirka (1995, 1997). They categorized the possible wake structure according to: a vortex street; an unsteady bubble; and a steady bubble in the near-wake region. For the latter two categories, large-scale vortex formation is suppressed. Particularly relevant to the present work is the form of the unsteady bubble, which, according to dye injection, could exhibit a varicose, as opposed to sinuous, instability mode of the shear layers separating from the cylinder. The agglomerations of dye into small-scale concentrations, in phase with respect to the plane of symmetry of the cylinder, are clearly evident in figures 10 and 13 of Chen & Jirka (1995).

All of the aforementioned unstable and stable modes of the near wake exist in the presence of a horseshoe vortex system about the fore surface of the vertical cylinder. Although the physics of this horseshoe vortex has not been characterized for the case of a shallow flow, considerable insight has been obtained for the case of a vertical blunt

obstacle or cylinder in a flow of large depth. Devenport & Simpson (1990) determined experimentally the turbulence characteristics and separation phenomena near a wing–body junction. Visbal (1991) numerically calculated a variety of ordered patterns of horseshoe vortices at low Reynolds number. At a threshold value of Reynolds number, ordered unsteadiness of the vortex system was evident. Seal, Smith & Rockwell (1997) characterized the vortical flow pattern at the junction of a rectangular bluff body with the plate. The vortex system involved unsteady formation and translation of a vortex towards the body, which interacted with a sustained corner vortex. This process involved a well-defined frequency. Praisner *et al.* (1997) and Praisner, Sabatino & Smith (2001) characterized the structure of the horseshoe (necklace) vortex about the leading portion of a wing–plate junction and its relationship to the surface heat transfer. These investigations are complemented by the study of Seal & Smith (1999), involving hydrogen bubble visualization of intertwining horseshoe (necklace) vortices at a cylinder–plate junction. Lawless, Lane & Best (2003) defined the junction vortex system past a surface-mounted cuboid and cylinder, with emphasis on the instantaneous patterns of flow structure. They found that the junction region involves a highly dynamic vortex system; the primary vortex exhibited an aperiodic orbital motion, in conjunction with patterns of unsteady flow down the face of the obstacle. Assessments of recent advances in our understanding of juncture flows are provided by Simpson (2001) and Lawless *et al.* (2003).

1.2. *Unresolved issues*

Shallow laminar inflow past a vertical cylinder is expected to give rise to instabilities/transition phenomena in the horseshoe (necklace) vortex system about the fore part of the cylinder, as well as in the near wake, provided the Reynolds number is sufficiently high. These phenomena and their inter-relationship appear not to have been investigated. Furthermore, concepts for their control have not been pursued. More specifically, the unclarified issues are as follows:

(i) The essential features of the instability of the horseshoe vortex system in a shallow laminar flow have not been characterized in terms of patterns of instantaneous streamline topology immediately adjacent to the bed, and the manner in which this topology changes with time. Furthermore, the corresponding spectral content of the near-bed velocity fluctuations, involving the frequency(ies) and amplitude(s) of the predominant spectral peaks, is unknown.

(ii) The instability/transition of the shear layer separating from either side of the cylinder may give rise to well-defined vortical structures, even when the large-scale Kármán mode is suppressed due to bed friction effects. The manner in which these vortical structures develop has not been characterized in relation to: (*a*) the vorticity layer separating from the cylinder; and (*b*) the multiple vorticity layers associated with the horseshoe (necklace) vortex system. Furthermore, the spectral content associated with the development of these vortical structures is unknown.

(iii) When the large-scale Kármán mode, as well as other possible modes of vortex formation, is suppressed in a shallow flow due to bed friction effects, controlled small-amplitude perturbations of the cylinder may give rise to well-defined vortical structures. This type of control of shallow wake flows has not been pursued.

The overall aim of the investigation is to address these aspects using a cinema technique of high-image-density particle image velocimetry, which provides wholefield patterns of the flow structure in conjunction with global spectral analysis over entire planes of the flow.

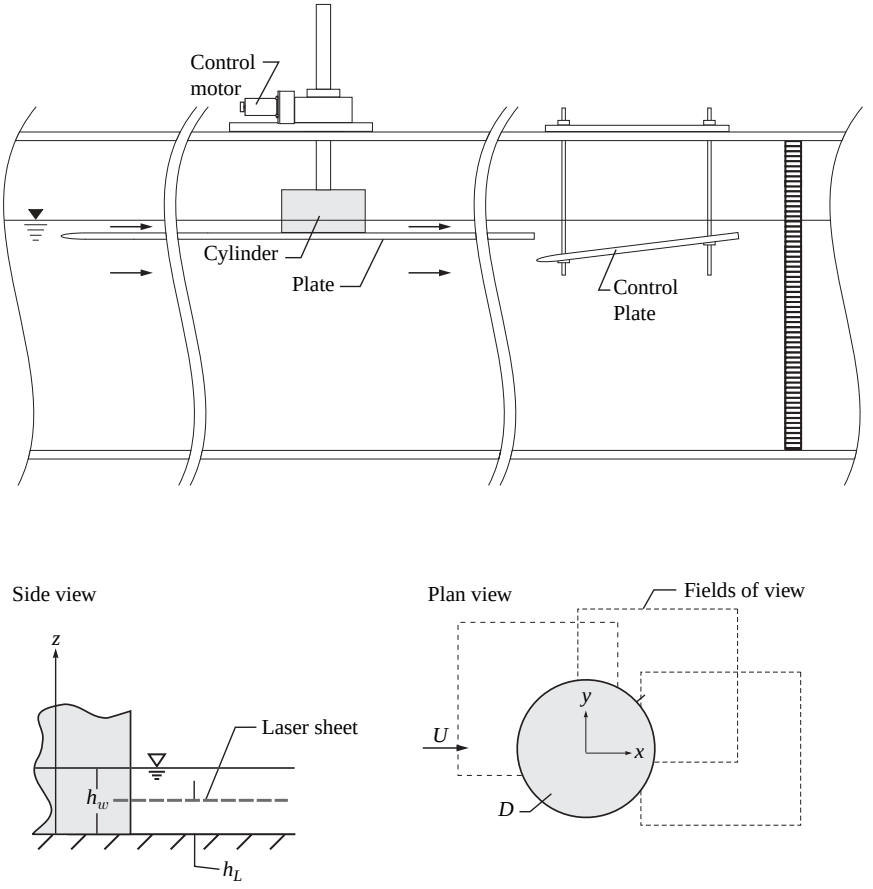

FIGURE 1. Overview of the experimental system and plan and side views of the cylinder–plate arrangement.

2. Experimental system and techniques

Experiments were conducted in a custom-designed recirculating free-surface water channel located in the Fluid Mechanics Laboratories at Lehigh University. The main test section is preceded by a large reservoir, in which flow conditioning occurs, following by a 3:1 contraction. The test section had a total length of 4318 mm, a width of 610 mm, and a depth of 610 mm.

As shown at the top of figure 1, a 12.7 mm thick plate with an elliptical leading edge, a width of 610 mm, and a length of 3660 mm was elevated 254 mm above the floor of the main test section of the channel. A cylinder of diameter $D = 101.6$ mm was positioned a distance of 3048 mm from the leading edge of the plate. A tiltable control plate was located at the trailing edge of the long horizontal plate, in order to precisely position the location of the stagnation point at the elliptical leading edge of the plate. This arrangement generated a well-defined shallow laminar approach flow.

Close-ups of the plan and side views of the cylinder–plate arrangement are given in the schematics at the bottom of figure 1. The shallow layer of depth $h_w = 6.3$ mm had a Reynolds number based on water depth h_w and velocity U of the free surface of $Re_{h_w} = 410$ to 820. The depth h_w normalized by the diameter D was $h_w/D = 0.0625$, thereby satisfying the condition $h_w/D \ll 1$ for existence of a shallow wake. Over the

U (mm s^{-1})	U_a (mm s^{-1})	Re_{h_w}	Re_D	S	Fr
65.0	43.4	410	4400	0.23	0.17
76.8	51.1	485	5200	0.20	0.21
86.3	57.5	545	5800	0.18	0.23

TABLE 1. Experimental parameters for shallow flow ($h_w = 6.3$ mm) past a cylinder ($D = 101.6$ mm).

range of Reynolds number employed in this investigation, the laminar shallow layer incident upon the cylinder is fully developed, in view of the relatively long approach length $L/h_w = 484$ from the leading edge of the plate. The aforementioned range of Reynolds number based on h_w corresponds to a range of $Re_D = 4400$ to 8800 based on cylinder diameter D and depth-averaged velocity U_a.

The stability parameter S of the near wake, defined in § 1.1, provides an indication of whether or not large-scale vortex formation will be self-sustaining. This form of S was put forth by Ingram & Chu (1987). It has been assessed in the context of unstable and stable modes and the global (absolute) versus convective instability of the near wake by Chen & Jirka (1995, 1997). For the present investigation, dye visualization and quantitative imaging of the near-wake structure shows that the large-scale mode of vortex formation is completely suppressed for values of $S = 0.13$ to 0.23. These values correspond to values of Reynolds number, as indicated in the foregoing of $8800 \geqslant Re_D \geqslant 4400$ and $820 \geqslant Re_{h_w} \geqslant 410$. Within the ranges of these parameters, however, the varicose mode of instability of the near wake undergoes transformation from an attenuated to a highly organized state. That is, the lowest Reynolds number $Re_D = 4400$ and $Re_{h_w} = 410$ case, corresponding to $S = 0.23$, showed suppression of all modes of instability, and increases of Re_D and thereby Re_{h_w} corresponding to decreasing S, yielded onset of the highly ordered varicose mode of instability. Although data were acquired over the foregoing range of Reynolds number, images are presented herein to characterize the central features of the transition process. These images involve the values of water depth h_w, inflow velocity U at the free surface, depth-averaged velocity U_a, Froude number $U/\sqrt{gh_w}$, Reynolds number Re_{h_w} based on water depth h_w and velocity U, and Reynolds number Re_D based on cylinder diameter D and velocity U_a, and the shallow flow stability parameter S. An overview of these parameters is given in table 1.

The major focus of the present investigation is on the characteristics of the near wake for the case of the stationary cylinder. In addition, the effects of rotational perturbations of the cylinder on the onset of instabilities of the suppressed near wake are addressed. Prescribed rotational motion of the cylinder, of amplitude A, was at the most sensitive frequency of either the separating shear layer or the large-scale (Kármán) mode of instability. The peak-to-peak amplitude $2A$ of the rotational motion corresponds to $2R\theta$, in which R is the radius of the cylinder and 2θ is the total angle subtended during the rotational oscillation. These perturbations were attained with a rotational control system driven by a computer-controlled motor.

During each phase of the investigation, a technique of high-image-density particle image velocimetry was employed to quantitatively characterize the flow physics. The flow was seeded with 14.6 micron metallic-coated hollow plastic spheres. A Nd:Yag dual pulsed laser (532 nm) system was employed to generate laser sheets of approximately 1.0 mm thickness via a combination of spherical and cylindrical

lenses. For plan views, the laser sheet was located parallel to the bed (bottom surface) at different heights $h_L/h_w = 0.08$, 0.5 and 0.92, in which h_L is the distance of the laser sheet above the bed and h_w is the height of the shallow layer. These elevations therefore correspond respectively to locations immediately adjacent to the bed, at the midplane, and at the free surface. In the vicinity of the bed, the flow structure is three-dimensional, due to the existence of the junction (horseshoe) vortices described in the Introduction. The location of the aforementioned laser sheet, i.e. plane of imaging, immediately adjacent to the bed surface, therefore indicates the footprint of the three-dimensional vortex system above the bed. The unsteady characteristics in this near-surface region are expected to directly indicate the time-dependent features of the vortex system.

Images were acquired using a CCD camera with a resolution of 1000×1016 pixels at a rate of fifteen frames per second, with a time delay between frames from 8 ms to 12 ms. The magnification factor was $M = 1{:}12.6$. It yielded fields of view 114 mm $\times$ 117 mm. In all cases, a total of 138 images were taken for each continuous run. A cross-correlation technique, using a 32×32 pixel interrogation window with a 50% overlap, was used to calculate the vector fields. This approach provided an effective grid size of 2 mm $\times$ 2 mm in the plane of the laser sheet. As a result, approximately 3480 velocity vectors were generated in the plan view. These velocity fields were then used to calculate instantaneous, phase-averaged and time-averaged patterns of vorticity, streamline topology and Reynolds stress correlation. Furthermore, since the images were acquired in a cinema mode at an effective framing rate of 15 frames per second, and the representative frequencies f_o of the unsteadiness were in the range $0.55 \leqslant f_o \leqslant 0.78$ Hz, it was possible to determine the time record at a given point in the flow field, then calculate the spectrum of the velocity fluctuation at that location. The spectral analysis was carried out using the standard definition and procedure for calculation of the auto-spectral density given by Newland (1993, p. 120). Correspondingly, cross-spectra, yielding spectral amplitudes and phase differences, could be determined between any two points in the flow field. Since a total of 3480 grid locations were available, it was possible to determine spectra and cross-spectra at a very large number of points in the flow field, all based on the same time record.

3. Instability of the separating shear layer in the near wake: coupling with the horseshoe (necklace) vortex instability

Figure 2 shows dye visualization of the instantaneous flow structure of the horseshoe vortex system about the upstream surface of the cylinder, as well as in the shear layer separating from the cylinder. The stability parameter, defined in the previous section, has a value $S = c_f D/h_w = 0.18$, which corresponds to suppression of the large-scale mode of vortex formation. Undulation of the horseshoe vortex pattern at frequency f_o, which is evident in the corresponding cinema sequence, is in accord with the instability of the separating shear layer at the same frequency f_o. In other words, the development of coherent vortical structures in the separating shear layer downstream of the cylinder cannot be considered in isolation from the unsteady three-dimensionality about the upstream surface of the cylinder, in contrast to the case of instabilities from a cylinder of very large aspect ratio. The frequency f_o can be scaled according to the displacement thickness δ^* of the boundary layer at a location immediately preceding the onset of separation that leads to formation of the horseshoe vortex system. Figure 2(*c*) shows the dimensionless frequency $f_o\delta^*/U$ versus Reynolds number $Re_{\delta*}$ based on displacement thickness δ^*. The results are

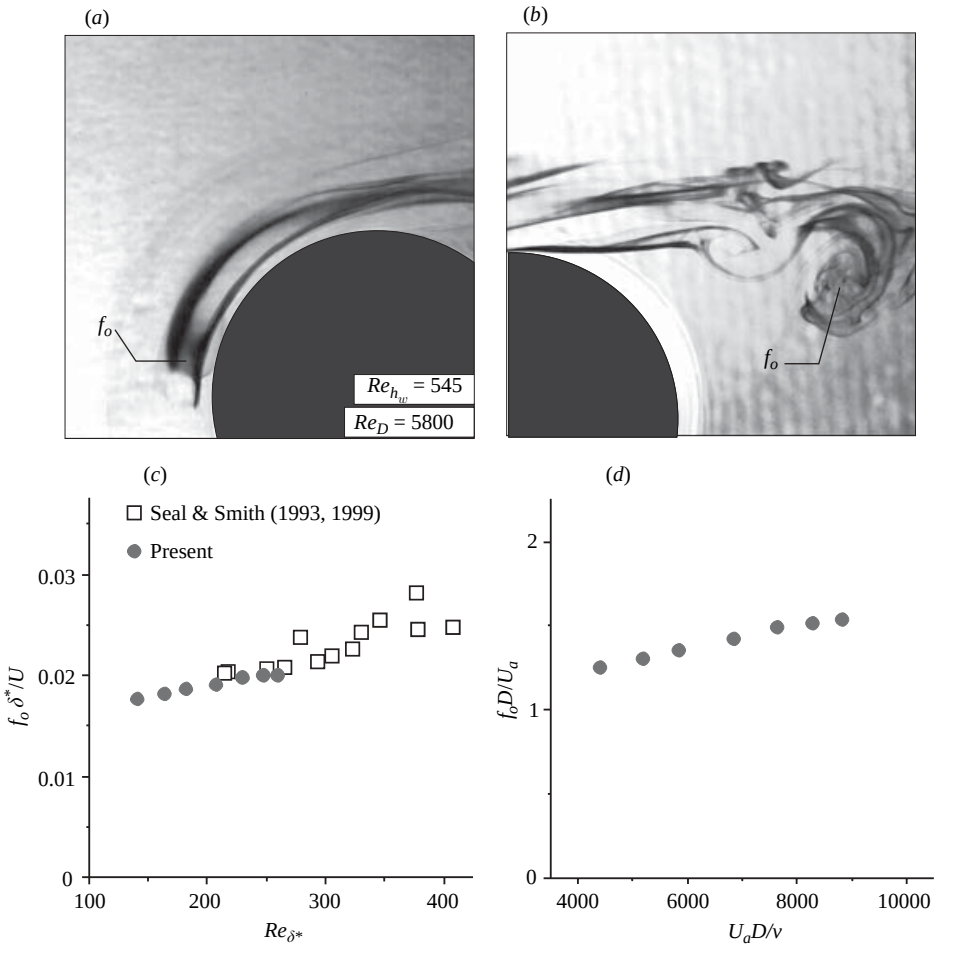

FIGURE 2. Visualization via dye, injected at the bed, showing unsteady horseshoe vortex (*a*) and vortex formation in the shear layer separating from the cylinder (*b*). Unsteadiness is at frequency f_o in both regions of flow. The stability parameter $S = 0.18$. Plots show: (*c*) dimensionless frequency $f_o\delta^*/U$ versus Reynolds number $Re_{\delta*}$ based on displacement thickness δ^* of the approach boundary layer immediately prior to separation and velocity U at edge of boundary layer; and (*d*) dimensionless frequency f_oD/U_a versus Reynolds number $Re_D = U_aD/\nu$, based on cylinder diameter D and velocity U_a averaged over thickness of shallow layer.

shown along with the data given in Seal (1993) and addressed in Seal & Smith (1999), who originally characterized the unsteadiness of this horseshoe vortex system in a relatively deep water layer. Over the range of $Re_{\delta*}$ of the present study, relatively mild variations of the dimensionless frequency $f_o\delta^*/U$ are discernible. The onset of instability of the horseshoe vortex system arises from separation of the boundary layer from the bed, which gives rise to an inflectional velocity distribution, and thereby promotes rapid amplification of disturbances. The frequency of this instability can also be scaled on the momentum thickness θ of the inflow layer, as described by Seal *et al.* (1997). The dimensionless frequency based on momentum thickness is in close agreement with that determined from linear stability theory.

Also shown in figure 2(*d*) is the dimensionless frequency of oscillation of the present data in the form f_oD/U_a versus Reynolds number $U_aD/\nu = Re_D$. Velocity U_a

is averaged over the depth of the shallow layer. These data points of figure 2 may be compared with the frequency of small-scale vortex formation in the separating shear layer from a cylinder of large spanwise extent, as described by Prasad & Williamson (1997):

$$f_{sl}/f_k = 0.0235 \times Re_D^{0.67} \tag{1}$$

in which f_{sl} and f_k are respectively the instability frequencies of the separating shear layer and the frequency of formation of classical Kármán vortices, which are suppressed in the present experiment due to bed friction effects. Over the range of $Re_D = 4400$ to 5800, for which images are compared herein, the maximum deviation from the correlation of equation (1) is 17%. It should be emphasized, however, that the vortex formation shown in figure 2 occurs in conjunction with a varicose instability of the entire near-wake region, which will be discussed in § 5. The preliminary dye visualization results of figure 2 served as the basis for detailed quantitative imaging, which is described in the figures that follow.

Images of the instability at frequency f_o in both the near-wake region and in the region about the upstream surface of the cylinder are given in figure 3 at a value of $Re_D = 5800$. The images are from a cinema sequence, where $N = 1$, 6 and 11 designate the frame numbers extracted for display. The top two rows of images show patterns of instantaneous streamlines s and surface-normal vorticity ω at an elevation immediately adjacent to the bed, i.e. $h_L/h_w = 0.08$. Consider the pattern of instantaneous streamlines at $N = 1$. A single saddle point S_a is clearly identifiable, whereas in subsequent images $N = 6$ and 11, two saddle points S_a, S_b and a node N_a are designated. The locations of the saddle S_a and node N_a undergo substantial streamwise excursion between images $N = 6$ and 11. Furthermore, detailed inspection of the patterns of merging streamlines about the shoulder of the cylinder shows significant variations in this region as well. These time-dependent variations in the streamline topology at the bed are reflected in discernible alterations of the instantaneous vorticity ω.

The lower two rows of images of figure 3(b) show the patterns of streamline topology s and surface-normal vorticity ω of the separating shear layers. The sequential development of well-defined concentrations of vorticity a and b is evident for increasing values of N. These concentrations are dominated by the negative (dashed line) vorticity of the shear layer separating from the cylinder, but regions of positive ω are drawn into the developing vortices a and b. This positive vorticity is from the horseshoe (necklace) vortex system and, in fact, it is possible to identify two sets of negative–positive layers of vorticity ω, exterior to the layer separating from the surface of the cylinder. These multiple layers are detectable in the images at all values of N.

Since the depth h_w of the shallow layer is small compared to the cylinder diameter D, i.e. $h_w/D = 0.0625$, one expects the general types of patterns shown in the bottom two rows of figure 3 to persist throughout the depth of the layer. Figure 4 compares patterns of instantaneous velocity $\boldsymbol{V}$, streamline s topology and vorticity ω at the free-surface, midplane and bed regions, corresponding respectively to $h_L/h_w = 0.92$, 0.5 and 0.08. Although the general features of the vortex formation are detectable at all values of depth h_L/h_w, the patterns of vortex formation, as well as the multiple layers of negative and positive vorticity of the horseshoe vortex system, are most distinctly defined at the bed, $h_L/h_w = 0.08$.

All of the foregoing images are instantaneous representations of the flow structure. Further insight is obtained by considering a time-average of a total of 138 images from the cinema sequence. Figure 5 shows averaged vorticity $\langle\omega\rangle$, root-mean-square transverse velocity fluctuation v_{rms}/U, and the Reynolds stress correlation $\langle u'v'\rangle/U^2$,

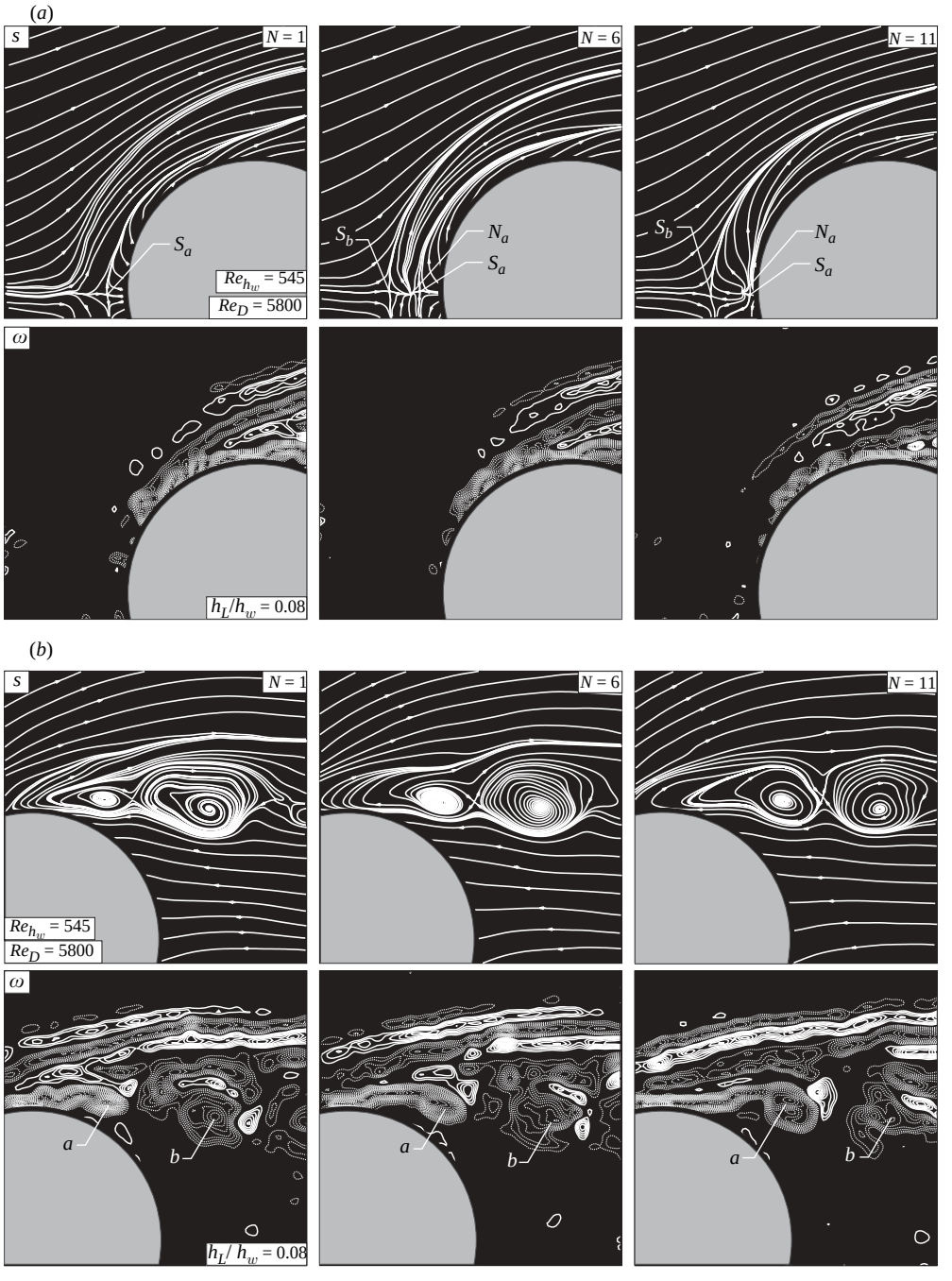

FIGURE 3. Instantaneous streamlines and vorticity patterns (*a*) at the surface of the bed, i.e. $h_L/h_w = 0.08$, in the region about the upstream surface of the cylinder and (*b*) in the near-wake region. The wake stability parameter $S = 0.18$. $N = 1$, 6 and 11 designate the frames extracted from a continuous cinema sequence. Near-wake streamline patterns are in a reference frame moving at one-half of the maximum velocity of the shallow layer. Positive and negative vorticity are represented by solid and dashed lines respectively. Minimum and incremental values of vorticity are $\omega_{min} = \pm 1\,\mathrm{s}^{-1}$ and $\Delta\omega = 1\,\mathrm{s}^{-1}$.

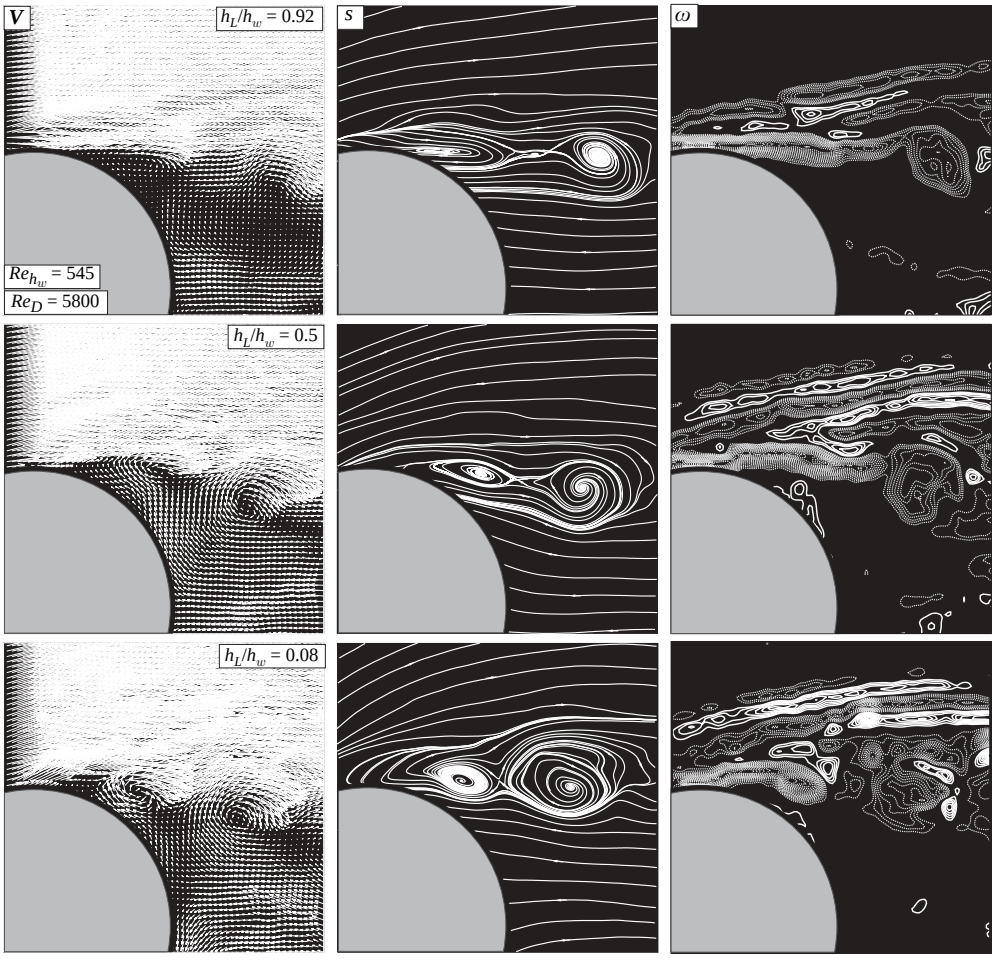

FIGURE 4. Comparison of instantaneous velocity $\boldsymbol{V}$, streamline topology s and vorticity ω at the free-surface, midplane and bed regions, corresponding respectively to $h_L/h_w = 0.92$, 0.5 and 0.08. Minimum and incremental values of vorticity are $\omega_{min} = \pm 1\,\mathrm{s}^{-1}$ and $\Delta\omega = 1\,\mathrm{s}^{-1}$.

in which U is the maximum velocity of the shallow layer. The patterns of $\langle\omega\rangle$ shown in the left-hand column indicate substantial levels for the shear layer immediately adjacent to the surface of the cylinder. On the other hand, the multiple layers of instantaneous vorticity ω exterior to this shear layer, evident in the right-hand column of figure 4, have either substantially reduced levels or are no longer discernible. This observation indicates that the unsteady fluctuations in spatial position of the multiple layers of the horseshoe vortex system result in considerably lower levels of time-averaged vorticity. The corresponding patterns of v_{rms}/U and $\langle u'v'\rangle/U^2$ indicate generally comparable levels at the bed and midplane, i.e. $h_L/h_w = 0.08$ and 0.5, with somewhat lower levels at the elevation of the free-surface $h_L/h_w = 0.92$.

4. Effect of Reynolds number on near-wake and horseshoe instabilities

Effects of decreasing the value of Reynolds number Re_D, below the value of 5800 shown in the previous images, are illustrated in figures 6 and 7. Figure 6 shows contours of constant amplitude of the spectral peak $|S_v(f_o)|$ for the horseshoe

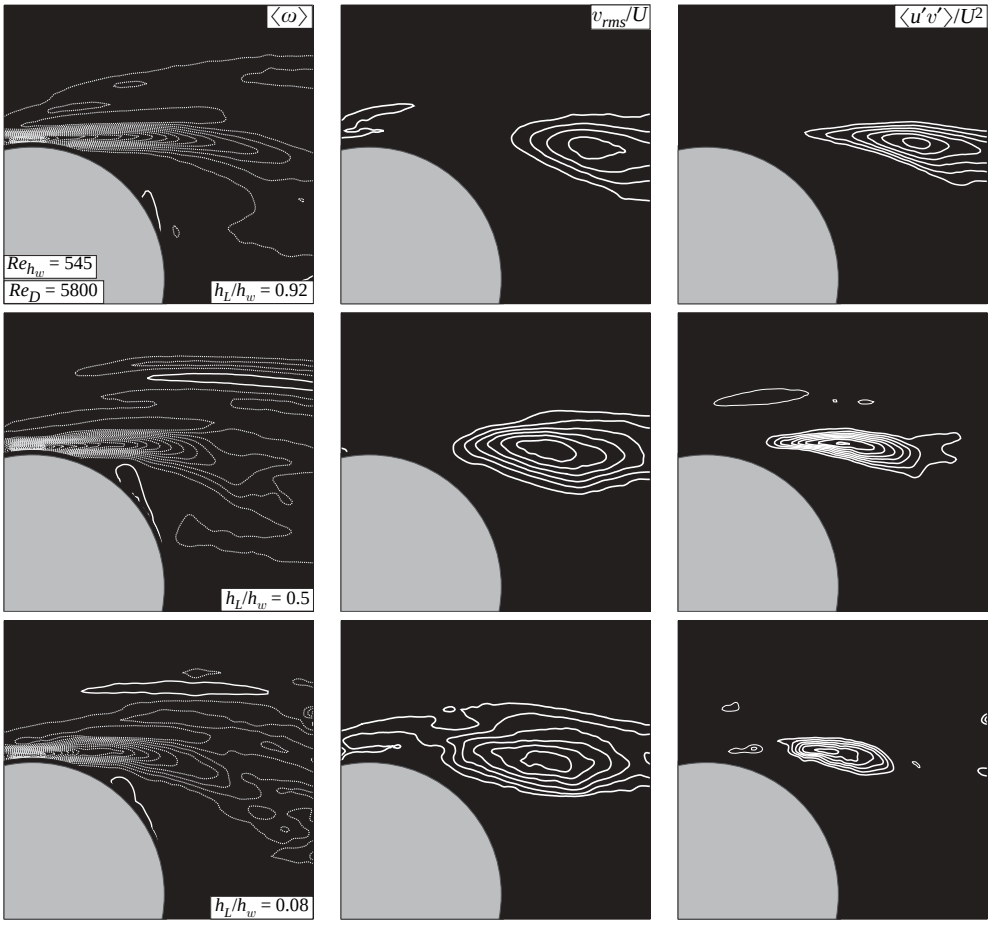

FIGURE 5. Comparison of time-averaged vorticity $\langle\omega\rangle$, root-mean-square transverse velocity fluctuation v_{rms}/U normalized by the maximum velocity U of the shallow layer, and the Reynolds stress correlation $\langle u'v'\rangle/U^2$ at elevations of $h_L/h_w = 0.92$, 0.5 and 0.08. The stability parameter $S = 0.18$. Minimum and incremental values are $\langle\omega\rangle_{min} = \pm 1\,\mathrm{s}^{-1}$ and $\Delta\langle\omega\rangle = 1\,\mathrm{s}^{-1}$, $[v_{rms}/U]_{min} = 0.06$ and $\Delta[v_{rms}/U] = 0.02$, $[\langle u'v'\rangle/U^2]_{min} = \pm 0.002$ and $\Delta[\langle u'v'\rangle/U^2] = 0.002$.

(necklace) and near-wake regions. Values of $|S_v(f_o)|$ are determined as follows. Using the cinema sequence of images, it is possible to track the time-dependent transverse velocity $v(t)$ at a large number of points over the field of view. For the top row of images of figure 6, a total of 3364 locations were tracked, whereas in the bottom row of images, 3480 points were monitored. Then, using these individual time records, it was possible to obtain the spectra $S_v(f)$, and thereby define the magnitude of the spectral peak at the frequency f_o, i.e. $|S_v(f_o)|$.

Contours of constant $|S_v(f_o)|$ for the horseshoe region indicate relatively low levels at $Re_{h_w} = 410$ and increasingly higher levels at 480 and 540. At the highest value of Re_{h_w}, substantial levels occur in the vicinity of the separation point. They represent particularly effective forcing of the separating shear layer. Representative spectra, corresponding to these contours of constant spectral amplitude are designated in the upper row of images of figure 6. For purposes of reference, spectra are shown in a region upstream of the cylinder (at the upper left of each image), and only very

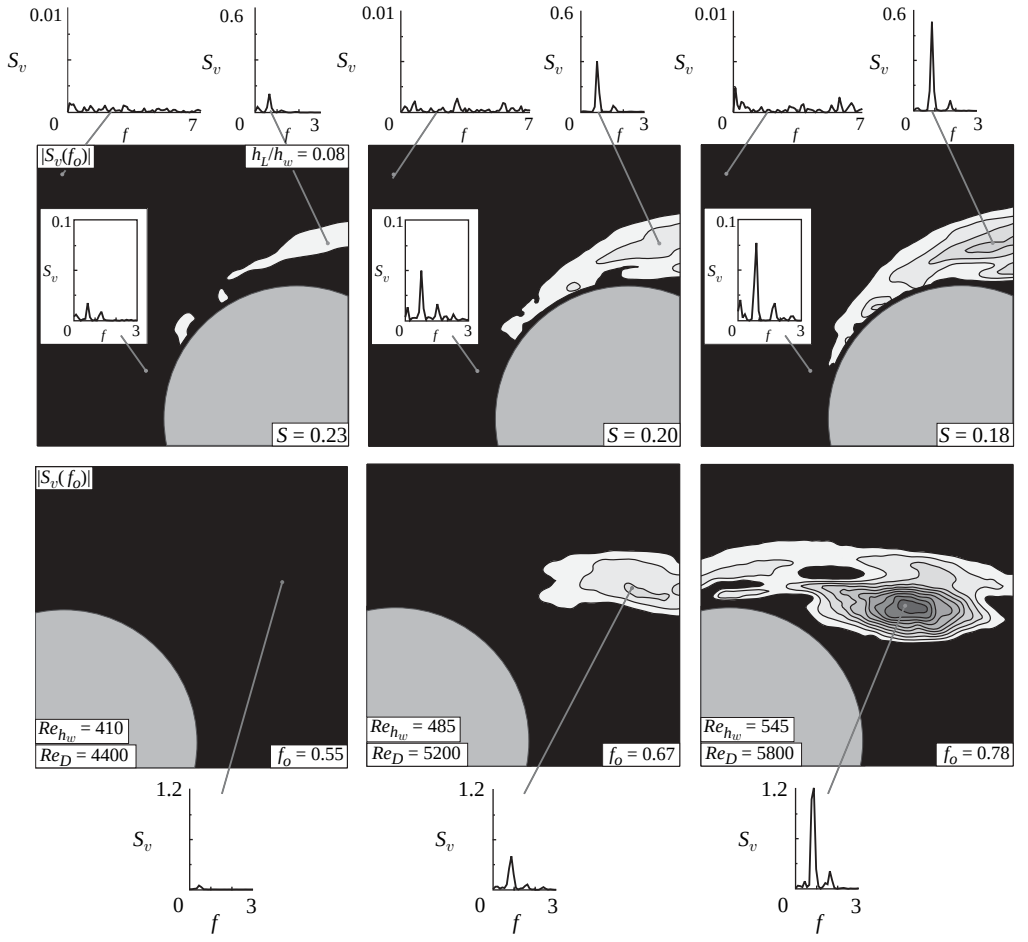

FIGURE 6. Contours of constant amplitude of the spectral peak $|S_v(f_o)|$ immediately adjacent to the bed $h_L/h_w = 0.08$ for the horseshoe (necklace) and near-wake regions with Re_D increasing from 4400 to 5800; correspondingly, the values of the stability parameter S are from 0.23 to 0.18. Minimum and incremental values of spectral amplitude are $[|S_v(f_o)|]_{min} = 0.1$ and $\Delta[|S_v(f_o)|] = 0.1$. Insets show selected spectra of transverse velocity $v(t)$ at locations designated.

low-level background noise is evident, due to the processing technique. At a location immediately upstream of the cylinder (close to its stagnation point), and at the lowest value of the Reynolds number $Re_{h_w} = 410$ ($Re_D = 4400$), the spectrum shows a well-defined peak and its first harmonic. It indicates the instability associated with the onset of boundary layer separation during formation of the horseshoe vortex, which is illustrated by the dye visualization of figure 2. As the Reynolds number progressively increases, corresponding to the middle and right images in the top row of figure 6, the peak spectral amplitude increases. Spectra in the shear layer separating from the shoulder of the cylinder, corresponding to the region at the upper right of each image of the top row of figure 6, exhibit spectral peaks that generally follow the increasing amplitudes of the aforementioned peaks of the horseshoe vortex system.

The $|S_v(f_o)|$ contours in the bottom row of figure 6 show nearly insignificant levels at $Re_D = 4400$, and with increases of Re_D to 5200, then 5800, relatively high values appear in a well-defined cluster immediately downstream of the separation. This

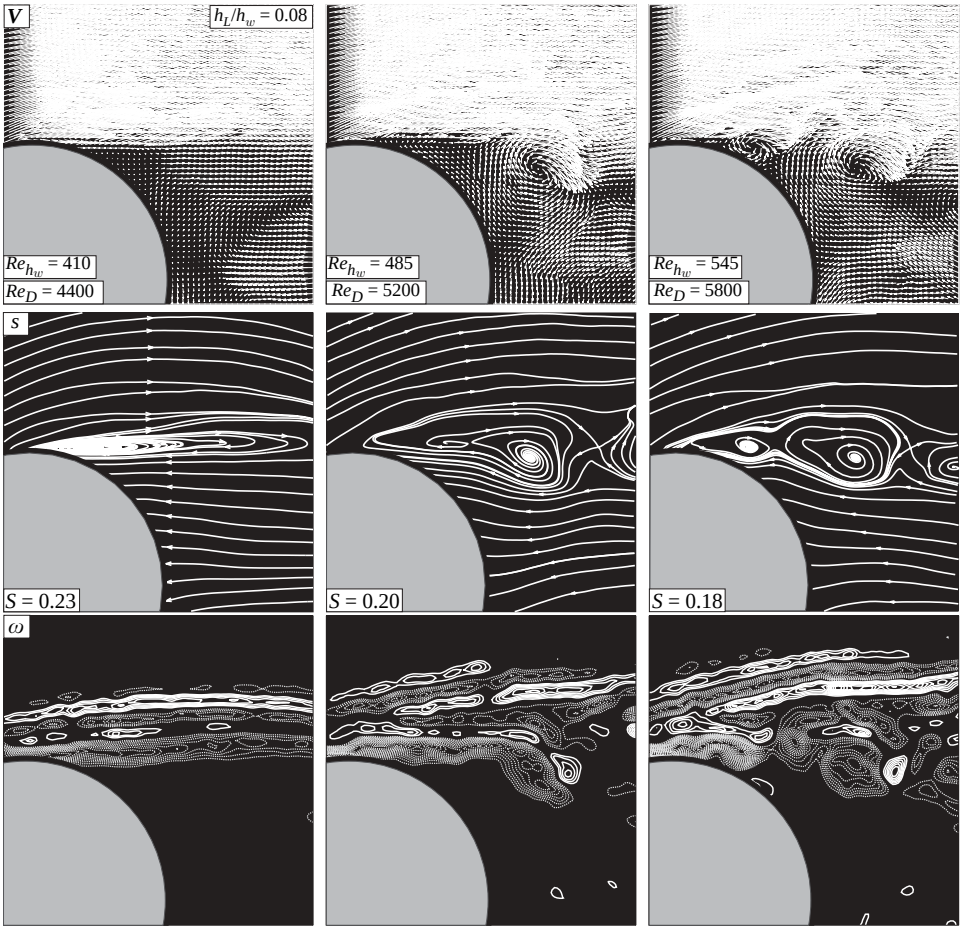

FIGURE 7. Patterns of instantaneous velocity $\boldsymbol{V}$, streamline topology s and vorticity ω immediately adjacent to the bed $h_L/h_w = 0.08$ in the near-wake region with Re_D from 4400 to 5800. Correspondingly, the values of the stability parameter S are from 0.23 to 0.18. Minimum and incremental values of vorticity are $\omega_{min} = \pm 1\,\mathrm{s}^{-1}$ and $\Delta\omega = 1\,\mathrm{s}^{-1}$.

observation is in accord with the pronounced concentrations of instantaneous vorticity ω evident in figures 3 and 4 at $Re_D = 5800$. Selected spectra, at the locations designated, show an increase in magnitude of the spectral peak, in accord with the spectra designated for the top row of images of figure 6.

Considering figure 6 as a whole, it is evident that the magnitude of the fluctuation at f_o of the horseshoe vortex system is directly linked to the magnitude of the fluctuation at f_o in the separating shear layer. When the undulations of the horseshoe vortex system are essentially stabilized at the lowest value of $Re_{h_w} = 410$ ($Re_D = 4400$), the instability of the separating shear layer is suppressed at the bed.

Further details of the near-wake structure over this range of Reynolds number are given in figure 7. At $Re_{h_w} = 410$ ($Re_D = 4400$), the patterns of instantaneous velocity $\boldsymbol{V}$, streamline s topology, and vorticity ω are relatively distributed, and as the value of Reynolds number increases, the onset of distinct concentrations, representative of the shear-layer instability, becomes increasingly evident.

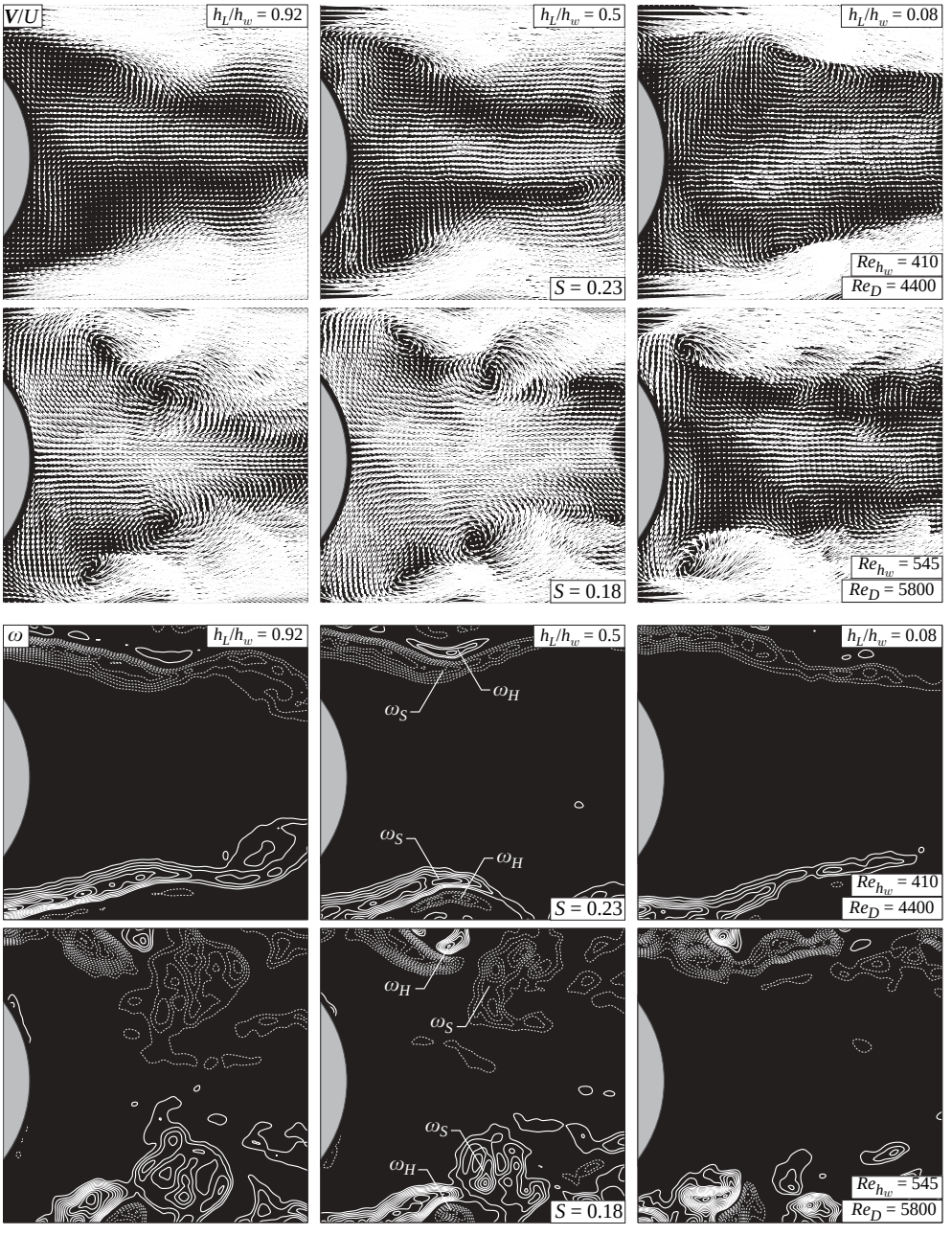

FIGURE 8. Patterns of instantaneous velocity $\boldsymbol{V}/U$ and vorticity ω showing instabilities from either side of the cylinder involving respectively vorticity ω_H and ω_S from the horseshoe vortex and separating shear layer at Reynolds numbers $Re_D = 4400$ and 5800, for elevations corresponding to the free-surface, midplane and bed regions, $h_L/h_w = 0.92$, 0.5 and 0.08. The values of stability parameter S are 0.23 and 0.18, respectively. Minimum and incremental values of vorticity are $\omega_{min} = \pm 2\,\mathrm{s}^{-1}$ and $\Delta\omega = 1\,\mathrm{s}^{-1}$.

5. Structure of instability across the near wake

Up to this point, the instability in a single shear layer from the cylinder has been addressed. Figure 8 focuses on the relationship between the instabilities from either

side of the cylinder at two representative values of Reynolds number $Re_D = 4400$ and 5800, for elevations corresponding to the free-surface, midplane and bed regions, $h_L/h_w = 0.92$, 0.5 and 0.08. The reader is referred to the images of figure 8 for corresponding values of Re_{h_w} and S.

Considering together the patterns of velocity $\boldsymbol{V}$ and vorticity ω at $Re_D = 4400$, the instability is substantially or completely suppressed at all elevations. Complete suppression appears to occur at $h_L/h_w = 0.08$, while at the midplane and free surface $h_L/h_w = 0.5$ and 0.92, detectable, but relatively low-level undulations are discernible. The distorted shear layers from the surface of the cylinder, indicated as ω_S, are accompanied by detectable regions of vorticity from the horseshoe system designated as ω_H, as shown in the image of ω at $h_L/h_w = 0.5$.

On the other hand, at $Re_D = 5800$, the patterns of $\boldsymbol{V}$ and ω indicate the rapid onset of focused swirl patterns of V and concentrations of ω at all elevations across the shallow layer. Pronounced concentrations of ω, which are associated with the separating shear layer ω_S, are particularly evident at higher elevations $h_L/h_w = 0.5$ and 0.92. In all cases, it is possible to detect vortical structures from the horseshoe system designated as ω_H.

A remarkable feature of all of the patterns of figure 8 is the fact that the developing shear layer systems from either side of the cylinder are mirror images of each other, with respect to the plane of symmetry of the cylinder. In other words, the developing instability, which is clearly evident at $Re_D = 5800$, is in the varicose mode, as opposed to a sinuous mode. An interesting feature of the patterns of velocity $\boldsymbol{V}$ at all elevations, but especially at the midplane and free surface, $h_L/h_w = 0.5$ and 0.92, are the relatively large magnitudes of velocity vectors oriented in the upstream direction along the centre of the wake. It is evident that this upstream-oriented volume flux through the central portion of the wake satisfies the entrainment demands of the rapidly developing unsteady shear layers on either side of the cylinder.

The development over time of the spatial patterns of vorticity are shown in figure 9 at the highest Reynolds number $Re_D = 5800$, for which the near-wake instability is well-defined. Sequences of images designated as $N = 1$, 5 and 9, which represent excerpts from the complete cinema sequence, are shown at three elevations, $h_L/h_w = 0.92$, 0.5 and 0.08, corresponding respectively to the plane immediately adjacent to the free surface, at the midplane and at the bed. Clusters of vorticity are identified according to whether they are associated with the agglomeration of vorticity ω_S of the shear layer or vorticity ω_H of the horseshoe vortex. To facilitate direct comparison, the time sequence of images at all elevations is presented in a phase-referenced fashion, whereby, for example, the predominant positive (solid line) vorticity concentration occurs at the same streamwise position for all elevations.

6. Response of attenuated instability to controlled perturbations

The consequence of small-amplitude perturbations applied to the attenuated instability of the near-wake region at $Re_D = 4400$ is given in figure 10. Amplitude A/D corresponds to the tangential amplitude of the cylinder oscillation, i.e. one-half the normalized peak-to-peak arc distance $2A/D$ subtended during a rotational oscillation cycle of the cylinder. These perturbations are applied at a frequency that yields the maximum response of the separated shear layer system. A range of frequency f_e was considered during preliminary experiments and it was found that a value $f_e D/U_a = 1.3$ was most effective. This value closely approximates the dimensionless frequency of the very low-level instability at elevations above the bed obtained from spectral

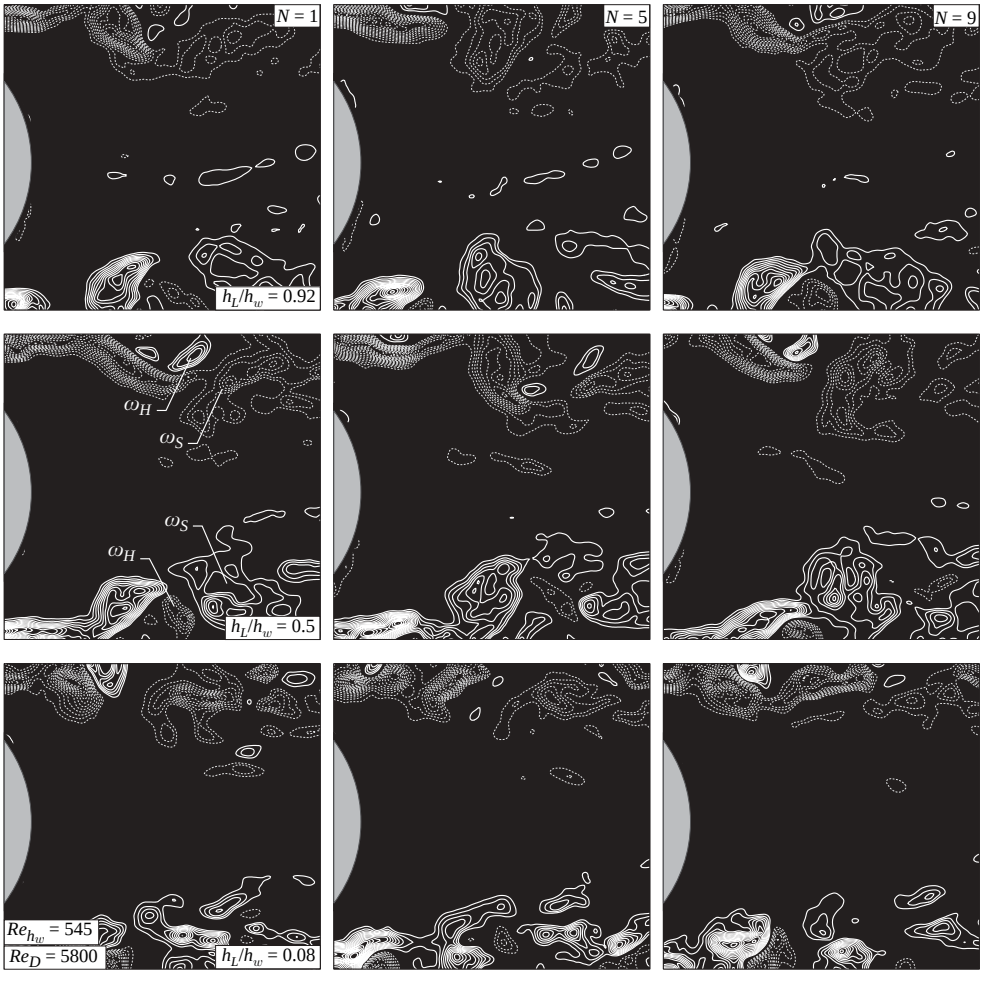

FIGURE 9. The onset and development of patterns of vorticity at Reynolds number $Re_D = 5800$ for elevations corresponding to the free surface, midplane and bed, i.e. $h_L/h_w = 0.92$, 0.50 and 0.08. The stability parameter $S = 0.18$. Minimum and incremental values of vorticity are $\omega_{min} = \pm 2\,\mathrm{s}^{-1}$ and $\Delta\omega = 1\,\mathrm{s}^{-1}$.

analysis of cinema images. As shown in figure 10, at this most sensitive frequency, a relatively low angular amplitude $A/D = 0.001$ produces a discernible effect on the system of vorticity layers, and as this amplitude level is increased to $A/D = 0.026$, the concentrations of vorticity are indeed pronounced and have a form similar to those naturally occurring at $Re_D = 5800$ in figures 3 and 4.

Comparison of instantaneous and averaged representations of the structure of the perturbed wake, for various values of amplitude A/D, are given in figure 11. For increasing A/D, the well-defined swirls of velocity vectors $\boldsymbol{V}$ and the associated concentrations of vorticity ω form closer to the surface of the cylinder. By comparing, for example, concentrations of vorticity from opposite sides of the cylinder, it is evident that they no longer are in an in-phase, or varicose, mode. Rather they are staggered, due to the nature of the rotational oscillation of the cylinder, which induces π-out-of-phase perturbations on either side of the cylinder.

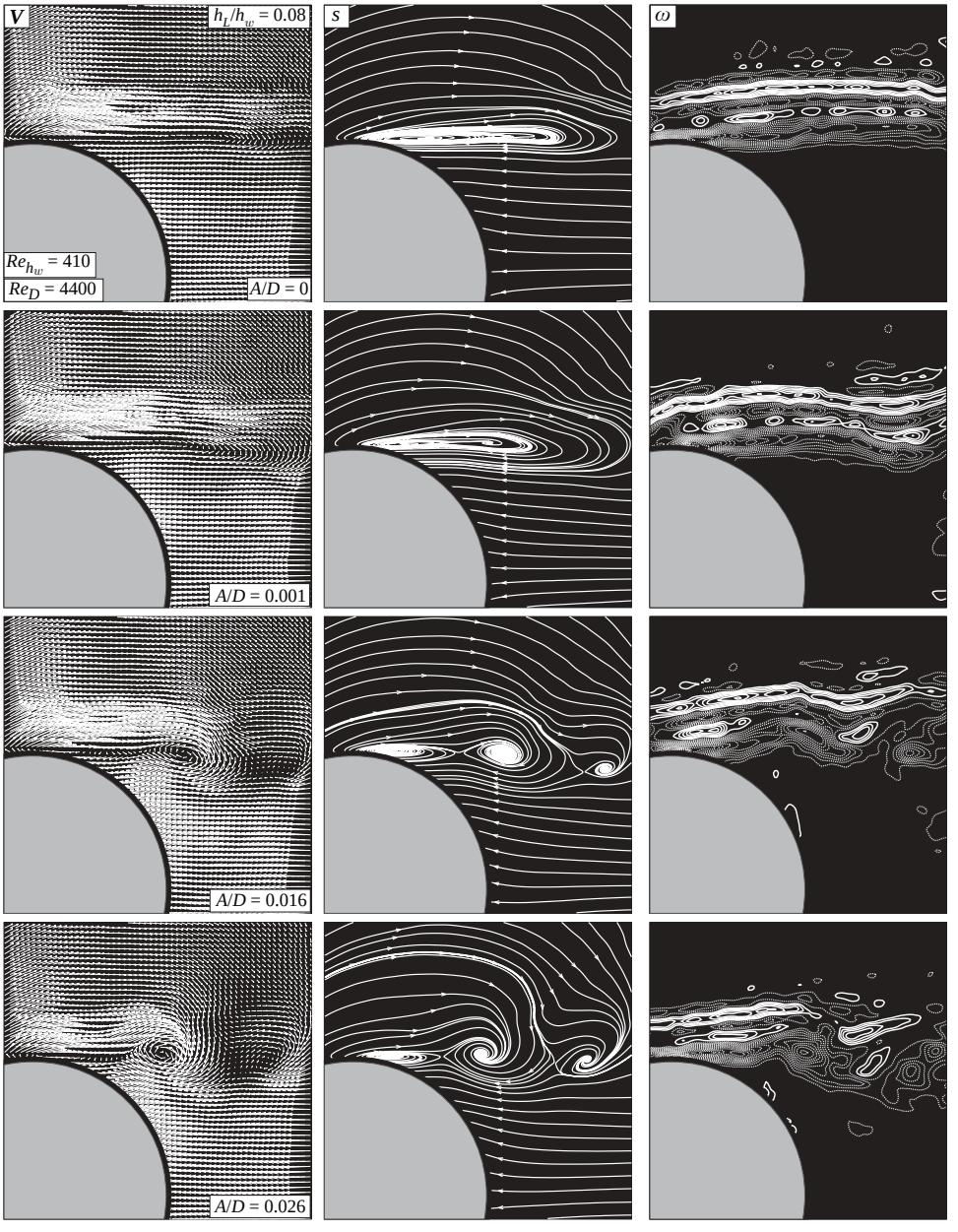

FIGURE 10. Consequence of small-amplitude angular perturbations at the most unstable shear-layer instability frequency f_o at $Re_D = 4400$. Instantaneous velocity $\boldsymbol{V}$, streamline topology s and vorticity ω are immediately adjacent to the bed, $h_L/h_w = 0.08$. Velocity and streamline patterns are in a reference frame moving at one-half of the maximum velocity of the shallow layer. The stability parameter $S = 0.23$. Minimum and incremental values of vorticity are $\omega_{min} = \pm 1\,\mathrm{s}^{-1}$ and $\Delta\omega = 1\,\mathrm{s}^{-1}$.

Also remarkable are the patterns of velocity vectors $\boldsymbol{V}$ within the central region of the wake, shown in the first row of images of figure 11. With increasing A/D, the magnitude of the upstream-oriented flow increases. This increase in upstream-oriented volume flux is in accord with an increase of the averaged transverse velocity

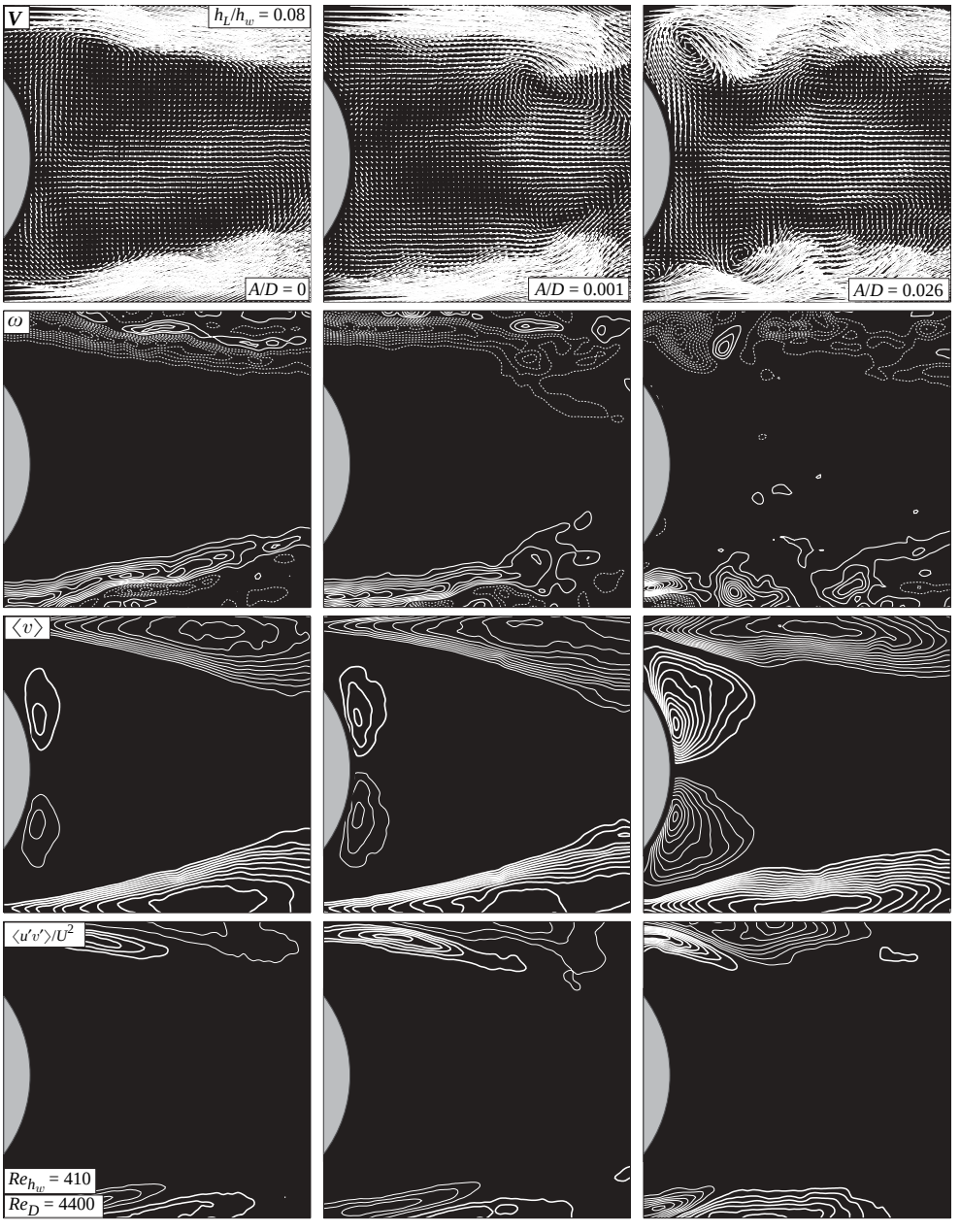

FIGURE 11. Patterns of instantaneous velocity $\boldsymbol{V}$ and vorticity ω, along with time-averaged transverse velocity component $\langle v \rangle$ and Reynolds stress correlation $\langle u'v' \rangle / U^2$ immediately adjacent to the bed, $h_L/h_w = 0.08$. Perturbations are at the most unstable frequency of the separating shear layer at $Re_D = 4400$. The stability parameter $S = 0.23$. Minimum and incremental values are $\omega_{min} = \pm 1\,\mathrm{s}^{-1}$ and $\Delta\omega = 1\,\mathrm{s}^{-1}$, $\langle v \rangle_{min} = 1.52\,\mathrm{mm\,s}^{-1}$ and $\Delta\langle v \rangle = 0.508\,\mathrm{mm\,s}^{-1}$, $[\langle u'v' \rangle / U^2]_{min} = \pm 0.002$ and $\Delta[\langle u'v' \rangle / U^2] = 0.002$.

$\langle v \rangle$, shown in the third row of images. It appears that this increase of $\langle v \rangle$ is associated with higher levels of Reynolds stress of the separating shear layer, which is shown in the fourth row of images; that is, increased Reynolds stress increases the entrainment to each of the shear layers.

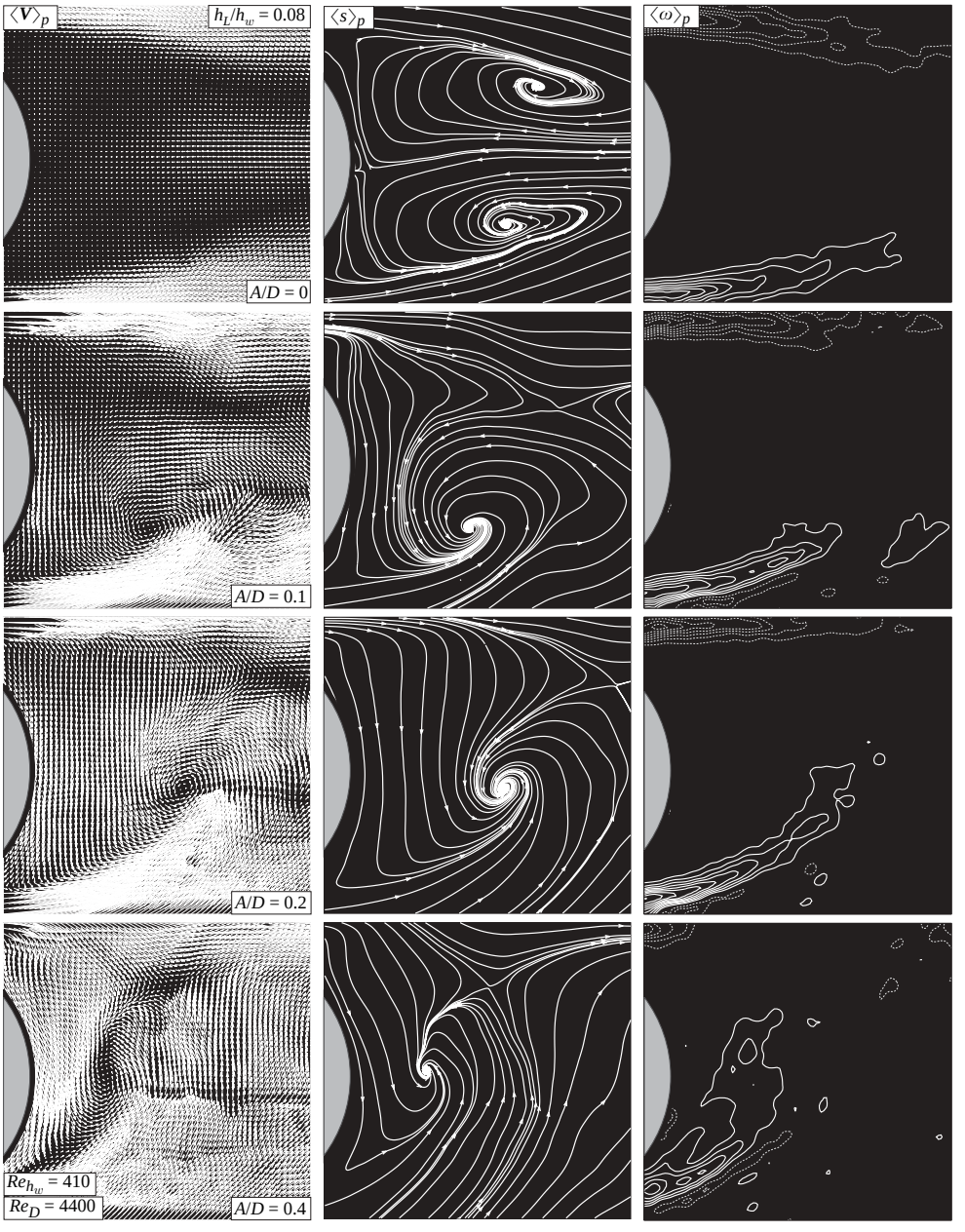

FIGURE 12. Phase-averaged velocity $\langle \boldsymbol{V} \rangle_p$, streamline topology $\langle s \rangle_p$, and vorticity $\langle \omega \rangle_p$ for perturbations at the expected frequency of large-scale Kármán vortex formation for various dimensionless angular amplitudes A/D. The stability parameter $S = 0.23$. Minimum and incremental values of vorticity are $[\langle \omega \rangle_p]_{min} = \pm 1\,\mathrm{s}^{-1}$ and $\Delta[\langle \omega \rangle_p] = 1\,\mathrm{s}^{-1}$.

If perturbations are applied at the expected frequency of large-scale vortex formation, designated as f_K, then the patterns at the bed take the form shown in figure 12. Considering, first of all, the patterns at $A/D = 0$, which represents the attenuated large-scale (Kármán) instability, the streamline $\langle s \rangle_p$ topology shows stationary cells

in the near wake, which have a form broadly similar to the steady recirculation cells that occur in the near wake of the cylinder of large spanwise extent at a much lower Reynolds number of the order of $Re_D = 60$. For values of $A/D = 0.1$, 0.2 and 0.4, large-scale vortex formation is indicated, and all streamline patterns show the same major critical points in the near-wake region. That is, a well-defined focus, which represents the apparent centre of the swirling streamline pattern, and a saddle point, which corresponds to the apparent intersection of streamlines, can be identified at each value of A/D. The vorticity layer forming from the bottom surface of the cylinder, shows increased deflection towards the centreline of the wake for increasing values of A/D.

Corresponding patterns of averaged Reynolds stress correlation $\langle u'v' \rangle / U^2$ are shown in figure 13 as a function of amplitude A/D of the cylinder rotation at various elevations of the bed, $h_L/h_w = 0.08$, 0.5 and 0.92. Irrespective of the elevation h_L/h_w, the consequence of increasing A/D is to increase the level of $\langle u'v' \rangle / U^2$. At higher values of A/D, pronounced concentrations of $\langle u'v' \rangle / U^2$ occur immediately adjacent to the base of the cylinder. At intermediate values of $A/D = 0.1$ and 0.2, cells of $\langle u'v' \rangle / U^2$ are formed in the region immediately downstream of the base of the cylinder. Large amplitudes of $\langle u'v' \rangle / U^2$ occur at the midplane and free surface, $h_L/h_w = 0.5$ and 0.92, especially for larger values of amplitude $A/D = 0.2$ and 0.4. It is evident, however, that at the bed, $h_L/h_w = 0.08$, these relatively high regions of $\langle u'v' \rangle / U^2$ are suppressed.

7. Concluding remarks

It is well known that the onset of a global instability, and thereby large-scale Kármán vortex formation in the near wake of a cylinder in shallow flow, can be attenuated by bed friction effects, provided the conditions of a stability parameter are satisfied. The present results indicate, however, that even when such suppression of the large-scale mode of vortex formation occurs, it is possible to witness a well-defined varicose mode of instability, which involves well-defined vortex formation in the near wake. Over the range of Reynolds numbers based on depth h_w of the shallow layer and the diameter D of the cylinder considered herein, this varicose mode transforms from an attenuated state to a highly coherent, self-excited state. The qualitative dye visualization of Chen & Jirka (1995) suggests that this type of varicose mode can also occur at much higher Reynolds numbers. It therefore appears to be an inherent, robust feature of the wake structure.

The instability of this small-scale mode in the near wake is related to an instability of the horseshoe vortex system about the fore region of the cylinder. That is, the same predominant spectral component exists in the unsteadiness of the horseshoe vortex as in the shear layers separating from the shoulder of the cylinder. Furthermore, as the amplitude level of the fluctuation in the horseshoe system increases, coherent vortical structures are formed earlier in the separating shear layers. Such vortex formation encompasses vorticity not only from the separating layer but also from the adjacent vorticity layers associated with the horseshoe vortex.

When both the large-scale sinuous (Kármán) mode and the varicose mode are suppressed in the bed region at low value of the Reynolds number, it is possible to destabilize the wake via small-amplitude rotational perturbations of the cylinder. When this destabilization occurs, there is pronounced volume flow in the upstream direction along the central portion of the near wake. Furthermore, such destabilization is associated with enhanced Reynolds stresses in the separating shear layers, and

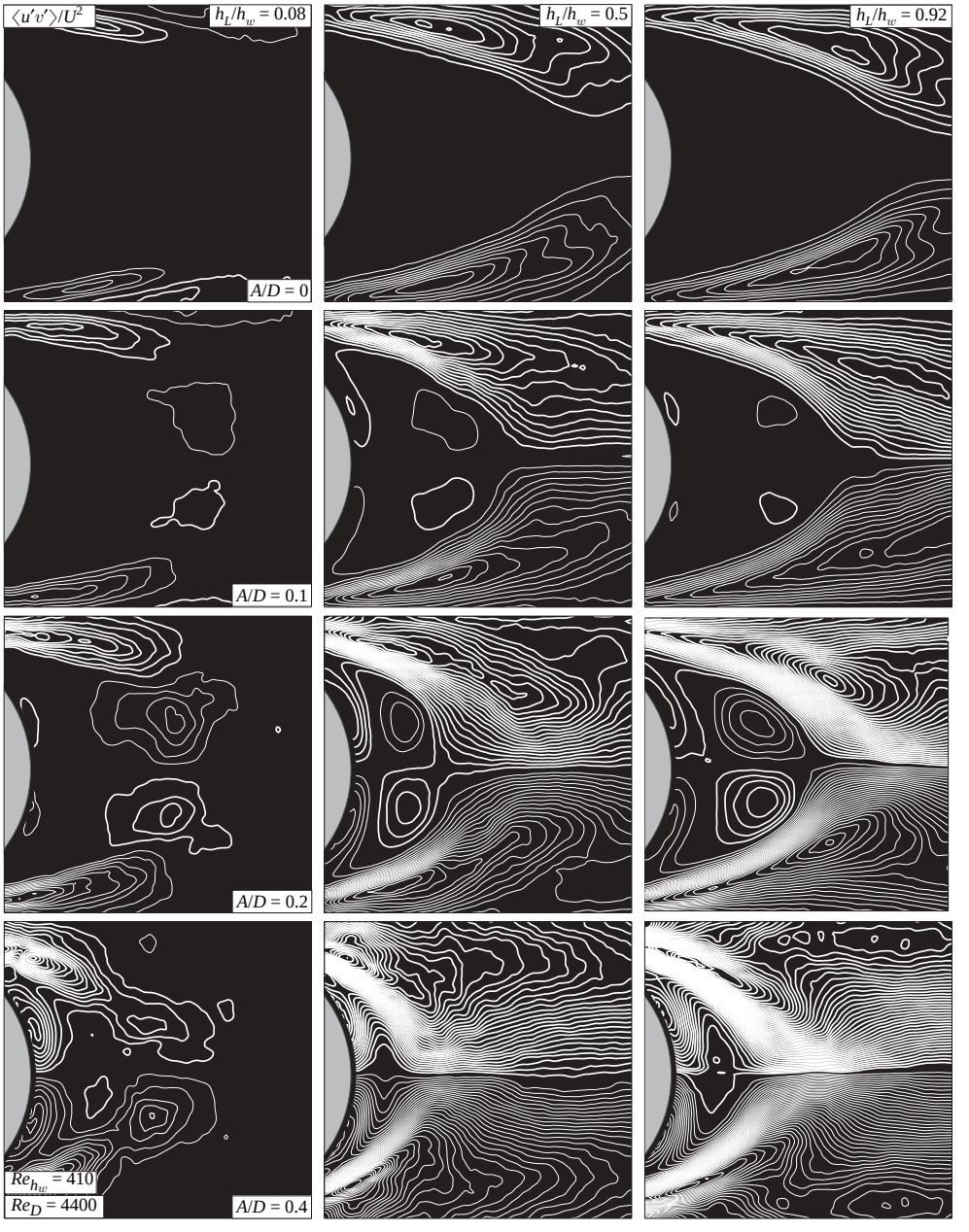

FIGURE 13. Patterns of averaged Reynolds stress correlation $\langle u'v' \rangle / U^2$ as a function of amplitude A/D of the cylinder rotation, at the elevations immediately adjacent to the bed, at the midplane and at the free-surface, $h_L/h_w = 0.08$, 0.5 and 0.92. The stability parameter $S = 0.23$. Minimum and incremental values of Reynolds stress are $[\langle u'v' \rangle / U^2]_{min} = \pm 0.002$ and $\Delta[\langle u'v' \rangle / U^2] = 0.002$.

thereby much larger values of transverse velocity towards the separating layers, especially near the base of the cylinder.

The aforementioned rotational perturbations can also be applied to the suppressed near wake at the frequency of inherent Kármán vortex formation, in order to induce

large-scale vortical structures. Patterns of Reynolds stresses in the wake take on various forms depending upon the excitation amplitude. Generally speaking, however, the magnitudes of these Reynolds stress correlations are significantly lower in the bed region. Furthermore, the locations of their peak values at the bed appear further downstream, compared to the locations of peaks at elevations above the bed.

The authors are pleased to acknowledge financial support of the National Science Foundation through Grant CTS-0228110, as well as supplemental support through the Office of Naval Research Grant N00014-94-1-0185.

REFERENCES

Akilli, H. & Rockwell, D. 2002 Vortex formation from a cylinder in shallow water. *Phys. Fluids* **14**, 2957–2967.

Balachandar, R., Chu, V. H. & Zhang, J. 1997 Experimental study of turbulent concentration flow field in the wake of a bluff body. *J. Fluids Engng* **119**, 263–270.

Balachanadar, R., Ramachandran, S. & Tachie, M. F. 2000 Characteristics of shallow turbulent near wakes at low Reynolds numbers. *J. Fluids Engng* **122**, 302–308.

Balachandar, R., Tachie, M. F. & Chu, V. H. 1999 Concentration profiles in shallow turbulent wakes. *J. Fluids Engng* **121**, 34–43.

Carmer, C. F. V., Rummel, A. & Jirka, G. H. 2002 Combined planar measurements of flow velocity and mass concentration in shallow turbulent flow. Part 2: Application of coupled PIV-PCA technique to turbulent shallow wake flows. *Proc. ASCE/IAHR Intl Conf. Hydraulic Measurements and Experimental Methods, Estes Park*, USA.

Carmer, C. F. V., Rummel, A. C. & Jirka, G. H. 2003 Influence of secondary motion in large-scale coherent vortical structures on the mass transport in a shallow turbulent wake flow. *Proc. IAHR/AIRH Intl Symp. Shallow Flows, Technical University of Delft, Netherlands, June 16–18*, Part 3, pp. 129–136.

Carmer, C. F. V., Weitbrecht, V. & Jirka, G. H. 2001 On the genesis and fate of large coherent vortical structures in turbulent shallow wake flows. *Proc. ISEH, IAHR 2001 Intl Symposium on Environmental Hydraulics, Tempe, USA.*

Chen, D. & Jirka, G. H. 1995 Experimental study of plane turbulent wakes in a shallow water layer. *Fluid Dyn. Res.* **16**, 11–41.

Chen, D. & Jirka, G. H. 1997 Absolute and convective instabilities of plane turbulent wakes in a shallow water layer. *J. Fluid Mech.* **338**, 157–172.

Chu, V. H., Wu, J.-H. & Khayat, R. E. 1983 Stability of turbulent shear flows in shallow channels. *Proc. 20th IAHR Congress, Moscow*, vol. 3, pp. 128–133.

Devenport, W. J. & Simpson, R. L. 1990 Time-dependent and time-averaged turbulence structure near the nose of a wing-body junction. *J. Fluid Mech.* **210**, 23–55.

Grubisic, V., Smith, R. B. & Schar, C. 1995 The effect of bottom friction on shallow-flow past an isolated obstacle. *J. Atmos. Sci.* **48**, 1985–2006.

Huerre, P. & Monkewitz, P. A. 1990 Local and global instabilities in spatially developing flows. *Annu. Rev. Fluid Mech.* **22**, 473–539.

Ingram, G. R. & Chu, V. H. 1987 Flow around islands in Rupert bay: an investigation of the bottom friction effect. *J. Geophys. Res.* **92** (C13), 14521–14533.

Kahraman, A., Sahin, B. & Rockwell, D. 2002 Control of vortex formation from a vertical cylinder in shallow water: Effect of localized roughness. *Exps. Fluids* **33**, 54–65.

Lawless, M. R., Lane, S. N. & Best, J. L. 2003 The junction vortex system: time-mean and instantaneous flow fields. *Proc. Intl Symp. Shallow Flows, Technical University of Delft, Netherlands, June 16-18*, Part 3, pp. 137–144.

Lloyd, P. M. & Stansby, P. K. 1997 Shallow water flow around model conical islands of small side slope. *J. Hydraul. Engng* **123**, 1057–1067.

Lloyd, P. M., Stansby, P. K. & Chen, D. 2001 Wake formation around islands in oscillatory laminar shallow-water flows. Part 1. Experimental investigation. *J. Fluid Mech.* **429**, 217–238.

Newland, D. E. 1993 *An Introduction to Random Vibrations, Spectral & Wavelet Analysis.* 3rd Edn, pp. 113–124. Longman.

Pattiaratchi, C., James, A. & Collins, M. 1986 Island wakes and headland eddies: A comparison between remotely sensed data and laboratory experiments. *J. Geophys. Res.* **92** (CI), 783–794.

Praisner, T. J., Sabatino, D. R. & Smith, C. R. 2001 Simultaneously combined liquid-crystal surface heat transfer and PIV flow-field measurements. *Exps. Fluids* **30**, 1–10.

Praisner, T. J., Seal, C., Takmaz, L. & Smith, C. R. 1997 Spatial-temporal flow-field and heat transfer behavior in end-wall junctions. *Intl J. Heat Fluid Flow* **18**, 142–151.

Prasad, A. & Williamson, C. H. K. 1997 Three-dimensional effects in turbulent bluff-body wakes. *J. Fluid Mech.* **343**, 235–265.

Schar, C. & Smith, R. B. 1993 Shallow-water flow past isolated topography. part II: transition to vortex shedding. *J. Atmos. Sci.* **50**, 1401–1412.

Scorer, R. S. 1978 *Environmental Aerodynamics.* Ellis Horwood Ltd., Chichester.

Seal, C. V. 1993 Experimental investigation of the laminar necklace vortex system for a rectangular block-flat plate junction. MS Thesis, Department of Mechanical Engineering, Lehigh University.

Seal, C. V. & Smith, C. R. 1999 Visualization of a mechanism for three-dimensional interaction and near-wall eruption. *J. Fluid Mech.* **394**, 193–203.

Seal, C., Smith, C. R. & Rockwell, D. 1997 Dynamics of the vorticity distribution in end-wall junctions. *AIAA J.* **35**, 1041–1047.

Simpson, R. L. 2001 Juncture flows. *Annu. Rev. Fluid Mech.* **33**, 415–443.

Smith, R. B. & Grubisic, V. 1993 Aerial observations of Hawaii's wake. *J. Atmos. Sci.* **50**, 3728–3750.

Tachie, M. F. & Balachandar, R. 2001 Shallow wakes generated on smooth and rough surfaces. *Exps. Fluids* **30**, 467–474.

Visbal, M. R. 1991 Structure of laminar juncture flows. *AIAA J.* **29**, 1273–1282.

Williamson, C. H. K. 1996 Vortex dynamics in the cylinder wake. *Annu. Rev. Fluid Mech.* **28**, 477–526.

Wolanski, E., Imberger, J. & Heron, M. L. 1984 Island wakes in shallow coastal waters. *J. Geophys. Res.* **89** (C6), 10553–10569.